SAND2018-1363J

A Numerical Model of Exchange Chromatography Through 3D Lattice Structures

Maher Salloum*,[1] and David B. Robinson[2]

January 22, 2018

*,[1] (Corresponding author) Sandia National Laboratories, 7011 East Ave., MS 9158, Livermore, CA 94550, USA, Email: mnsallo@sandia.gov, Phone: 925-294-2585

[2] Sandia National Laboratories, 7011 East Ave., MS 9161, Livermore, CA 94550, USA, Email: drobins@sandia.gov, Phone: 925-294-6613

Abstract

Rapid progress in the development of additive manufacturing technologies is opening new opportunities to fabricate structures that control mass transport in three dimensions across a broad range of length scales. We describe a structure that can be fabricated by newly available commercial 3D printers. It contains an array of regular three-dimensional flow paths that are in intimate contact with a solid phase, and thoroughly shuffle material among the paths. We implement a chemically reacting flow model to study its behavior as an exchange chromatography column, and compare it to an array of one-dimensional flow paths that resemble more traditional honeycomb monoliths. A reaction front moves through the columns and then elutes. The front is sharper at all flow rates for the structure with three-dimensional flow paths, and this structure is more robust to channel width defects than the one-dimensional array.

1 Introduction

Chromatography is a technology found in many industrial applications such as mixture analysis, bulk separation and ion exchange (*e.g.* water softeners). Chromatography involves the flow of a fluid around a stationary solid such that a reaction takes place resulting in mass exchange between the fluid and the solid. Chromatography column design aims to achieve tight reaction peaks or fronts with short times and short columns. The case of a second-order chemical reaction between the solid and fluid phases can result in a theoretically infinitely sharp reaction front that does not broaden as it progresses [1], although broadening mechanisms do occur in practice, and are easily studied [2–5]. The ability to minimize the broadening mechanisms is limited by the range of structures that can be fabricated [6].

Chromatography columns are usually constituted of randomly packed powders. Despite the successful operation of such chromatography systems, several disadvantages are encountered in packed powders. There is limited ability to modify designs to achieve theoretically optimal performance. Pressure drops required for flow in the column are likely to be higher than optimal, and high pressure drops can increase sensitivity to defects. Though the manufacturing process is mature and reliable in some cases, the non-deterministic nature of powder synthesis and packing can result in varying performance between columns or powder batches [7]. Modeling of packed powders usually involves use of Darcy's law, which uses a small number of empirical parameters to describe flow rate as a function of pressure, and offers little insight into the dependence of the performance of a chromatography column on how it is packed [8]. Modeling flow in the interstices of a large number of packed particles would be a challenging and computationally expensive task.

Replacing randomly packed powders by deterministically fabricated devices with optimized geometries has achieved major performance and efficiency improvements in some applications. Notable examples can be found in chromatography [3], planar chromatogra-

phy [9], microfluidic medical devices [10], microfluidic medical devices [11,12], and recently emerging "3D battery" structures [13].

These benefits of deterministic chromatography systems have been recognized in the early studies of Golay [3] where it was analytically proven that a symmetric one-dimensional (1D) tube can achieve an optimal efficiency. The benefits do not translate to preparative (high molar throughput) chromatography for bulk production when scaled up as arrays of 1D tubes [14]. However, deterministic 3D structures are more promising, as shown in the recent studies and reviews of Desmet *et al.* [6, 15, 16] who proposed high aspect ratio logpile structures to homogenize the flow in liquid chromatography, and noted the need to manufacture with the highest possible spatial resolution.

We see additive manufacturing (roughly synonymous with 3D printing) as a means to achieve deterministic structures, mainly because it allows wider design capabilities. It was noticed in [15] that periodic square and cubic structures and logpiles are obvious and suitable for a deterministic chromatography column geometry. Cubes and logpiles are ideal structural units when using additive manufacturing methods near their spatial resolution limit, because they typically print one horizontal layer at a time using cubic voxels or rastered lines. Logpile structures made by rastered lines have been studied as seawater salt extractors [17] and gas sorbents [18]. Additive manufacturing has recently been explored for chromatography columns [19, 20] by building porous beds with packed powders of spherical, tetrahedral, etc. particle shapes. The bed performance was experimentally found to have significant dependence on the different particle shapes and spacing configurations considered in the study.

In our study, we follow a different approach from the direct additive manufacturing of particle beds. Instead, we seek to generalize the 1D tube model of Golay into 3D. For instance, a straightforward 3D design would be to draw parallel tubes in one bulk chromatography column. Previous studies have shown that such simple parallel arrays of tubes do not work well as an approach to preparative gas chromatography because slight

variations in the tube diameters result in significant differences in flow rate in different tubes [14]. We pursue the hypothesis that this problem can be overcome if a designed amount of shuffling of material between tubes can be arranged, within the constraints of 3D printing technology. A 3D-printed lattice structure would be one way to achieve this. Specific intersections between tubes can be incorporated into a design, and the tortuosity of the flow channels can be precisely defined.

We propose such a 3D structure that can be readily additively manufactured at high spatial resolution and which, although inspired by arrays of tubes, allows flow shuffling as proposed by Desmet *et al.* and maintains equal pressure drop along all flow paths. We describe this structure and compare its performance to an array of parallel tubes. Our test case is a numerical model of hydrogen and deuterium gas exchange in a metal hydride column using coupled reactive flow with diffusion and convection. We also study the effect of fabrication defects on the performance of our proposed 3D structure compared to parallel tubes.

2 Column Geometry

One goal of this study is to investigate the effect of the porous structure geometry in a column requiring interaction of gas- and solid-phase species. We consider the two column geometries depicted in Figure 1 which show the gas phase Ω_g (violet) and solid phase Ω_s (grey). In both geometries, the gas and solid phase volumes are equal. The first geometry in the top panel is formed by drawing columns of square section of size a in a solid such that they are parallel to the flow direction (z direction). In other words, the gas flow streamlines are parallel and are of equal length to the tubes in this case. We refer to this geometry as the parallel tubes geometry. A defect is manifested by the omission of a solid ligament separating two parallel gas columns as highlighted in blue in Figure 1. When this happens, a larger tube is formed and can be problematic in chromatography

operation as discussed later in this paper.

We propose a second geometry where we would like to simultaneously fulfill the following specifications:

1. A geometry that can be fabricated with high spatial resolution by additive manufacturing.

2. A solid geometry that allows shuffling the flow between different tubes such that in the presence of a defect, the flowing gas will still be able to mix in other voids and pores.

3. A geometry that ensures that the flow is uniform in the voids *i.e.*, that the pressure drop is uniform along all non-defective flow paths.

Such a geometry is displayed in the bottom panel of Figure 1. Conceptually, it is formed in two steps. First, a unit structure (shown on the top right) is defined as struts along the edges of a cube. The strut width is one quarter the cube edge length, resulting in equal volumes of solid and void. The unit structure is spanned as a regular 3D array in the (i, j, k) directions as shown on the left of the bottom panel. The optimal flow direction that guarantees an equal pressure drop in all directions is aligned with the $(1, 1, 1)$ orientation. Thus the second step in building the geometry is to rotate the 3D array as shown in the Figure 1 (bottom right) so that the $(1, 1, 1)$ orientation aligns with a conveniently defined flow axis (z in Figure 1). The projection of the rotated unit cube onto a plane perpendicular to the flow axis has a hexagonal envelope, and it is convenient to align a line including two opposite corners of the hexagon with another axis (x in Figure 1). The structure has a periodicity of $(2\sqrt{6}a_h, 2\sqrt{2}a_h, 2\sqrt{3}a_h)$. The array is then intersected with a prism that defines boundaries of a column that are parallel or perpendicular to the flow axis. It can be convenient to have some of the dimensions be a multiple of the periodicities. For our simulations, we chose a structure with a square cross section with dimensions $(10\sqrt{2}a_h, 10\sqrt{2}a_h, 20\sqrt{3}a_h)$. Since the parallel tubes geometry has these

same dimensions, and the gas and solid volumes are equal, it follows that $a = 2.5a_h$ (see Figure 1, top left). We used $a_h = 0.025$cm.

In this resulting 3D structure, the gas streamlines are not parallel to the flow direction and their length is greater than the column length L_t. We refer to this geometry as the 111 lattice geometry. In practice, this structure can be fabricated on a 3D printer that prints one horizontal layer at a time with either the k or z axis oriented vertically. Printing with the k axis vertical is likely to be best when a_h is near the resolution limit of the printer. We have published a report on fabrication methods applicable to a column, [21] and intend to separately report on experimental studies of these structures soon.

We have also considered modeling a version of the 3D structure where the unit cell edges are aligned with the flow axis. This results in many flow channels with stagnant flow, which is difficult to model. The parallel tubes geometry can be considered a modification of this case that eliminates stagnant flow channels. In addition to being easier to model, the parallel tubes geometry is expected to have improved performance versus a geometry with stagnant channels, and thus set a higher standard for comparison to the 111 lattice geometry.

We have selected the column width a_t and length L_t to satisfy the following conditions:

1. A minimum column length where a reaction front can form and move inside the column without being affected by the boundary conditions. We chose a length that keeps the cost of our simulations tractable.

2. Regular and structured intersections between the solid and gas phases for the 111 lattice (*e.g.* the star shape at the column outlet) in order to eliminate any irregularities in the resulting geometry that might give rise to highly localized and refined meshes. This is a key reason behind our choice of multiples of the periodicity along two axes.

At the inlet of each geometry ($z = 0$), we have added a thin block of thickness $L_t/40$ as part of the gas phase Ω_g. The goal of this block is to obtain a more uniform gas flow

at the column inlet. It also attenuates the numerical oscillations that arise at large gas velocities.

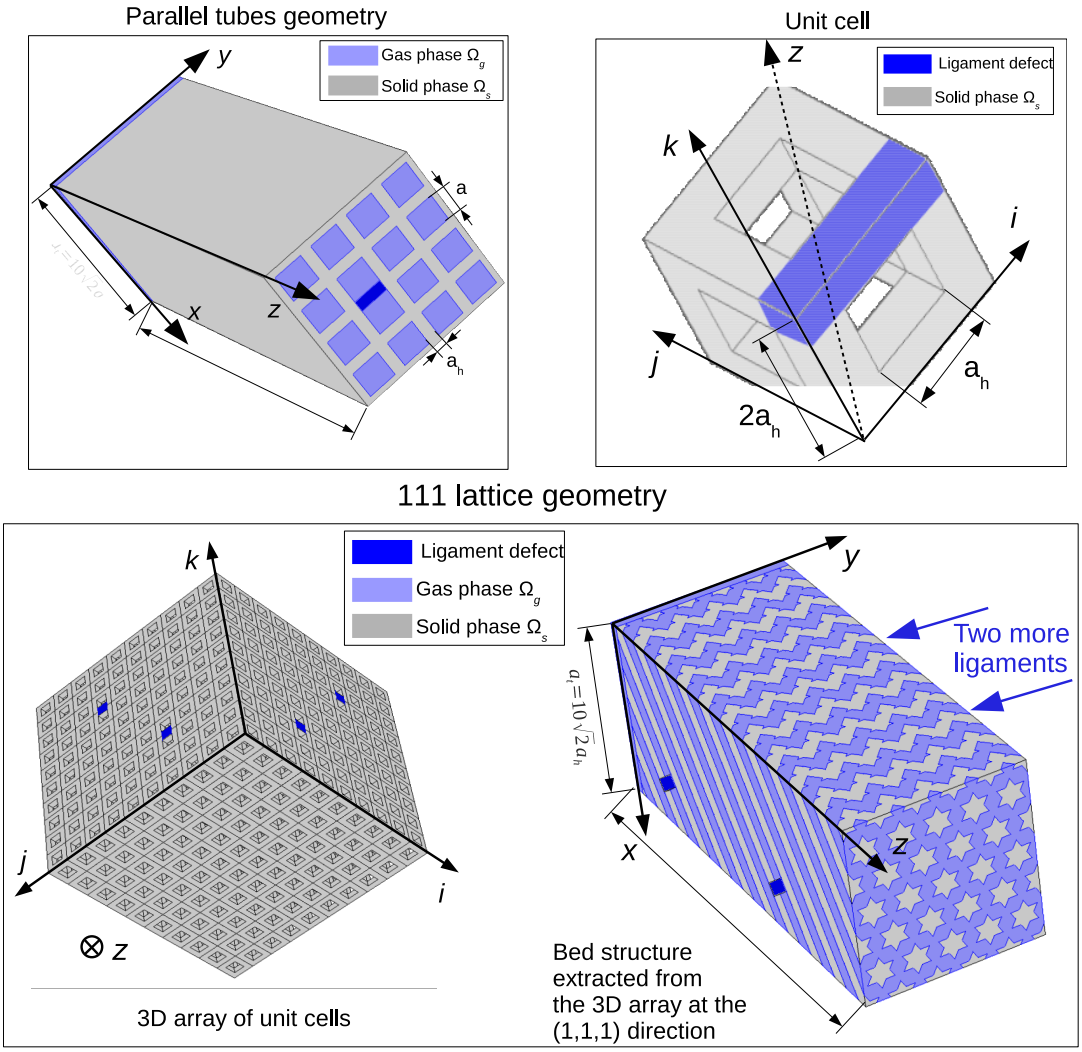

Figure 1: Depiction of the geometries used in the model simulation. (Top left) The parallel tubes geometry. (Top right) A unit cell of the 111 lattice. (Bottom) The 111 lattice geometry. Defect geometries are highlighted in dark blue.

2.1 Defects in the column Geometry

In our study, we also model the effect of defects in the column manufacturing process. We consider a_h as the minimum solid thickness that can be additively manufactured. Thus,

we assume that a manufacturing defect could occur when a solid ligament of thickness a_h is omitted. Such a defect is manifested in the parallel tubes geometry by eliminating the solid ligament in dark blue along the column length and including it in the gas phase as shown in the top of Figures 1 and 2. In the 3D structured column, we assume that a defect occurs in the column by omitting two pairs of isoplanar and perpendicular solid ligaments of size a_h in the (i, j) plane. Surface views of a defect are shown in dark blue in Figure 1, and interior views are shown in the bottom of Figure 2. The volumes of omitted solid material (*i.e.* considered as gas) per defect in both geometries are equal.

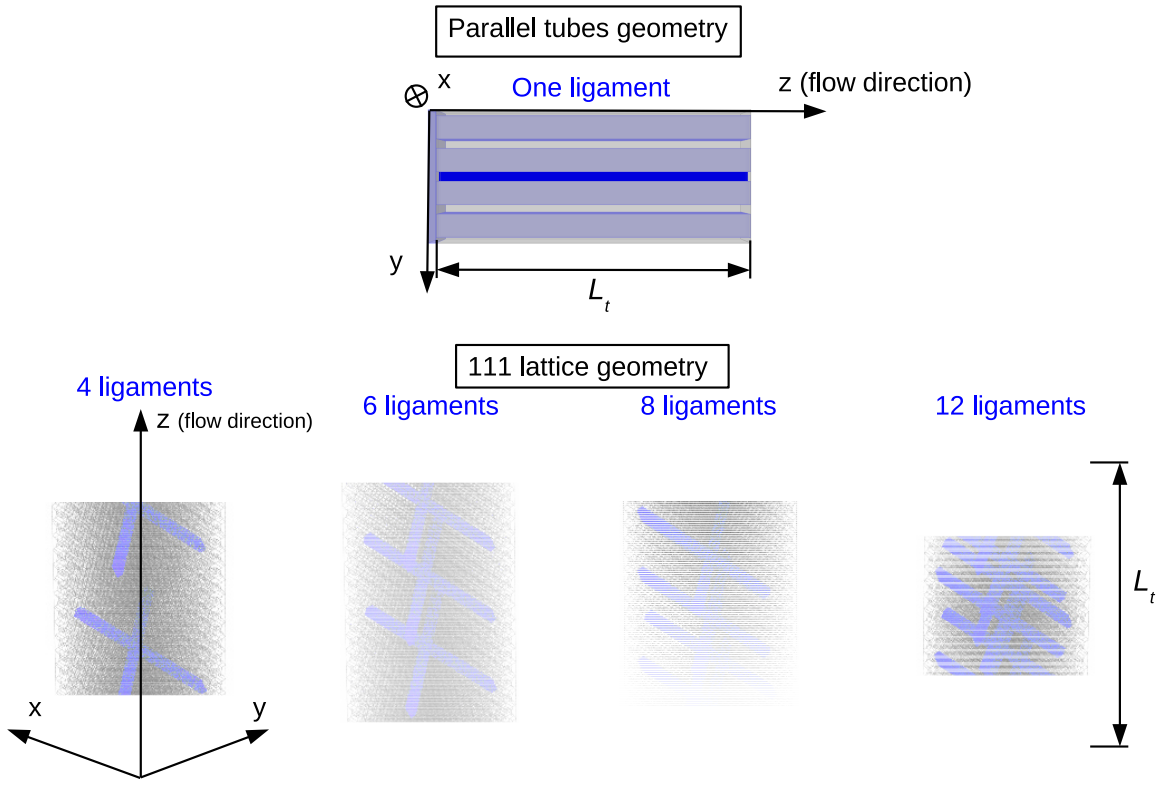

Figure 2: Further depiction of the defects in each geometry. (Top) Parallel tubes geometry. (Bottom) 111 lattice geometry, with varying numbers of defects.

3 Chemical Reactions

Several previous researchers have formulated hydrogen-deuterium exchange reaction models [22–25]. We use a simple model of the chemical reaction that is outlined in [5]. A pure gas-phase hydrogen isotope differing from that in the metal hydride enters the column at a given velocity through the thin square block as shown in Figure 1. As gas flows down the column, a chemical reaction occurs between the gas and the metal hydride, in which the initial isotope is displaced by the isotope that is flowing in. The gas flowing in is called the eluent, and the gas that is displaced from the solid and flows out is the eluate.

In this work, it is helpful to avoid the complications associated with the fact that gas-phase hydrogen is diatomic. However, it is valuable to predict the concentrations of the diatomic species, including mixed-isotope species such as HD. The differential equations presented in Section 4 of this paper will account for gas-phase hydrogen by atoms. The concentrations of the diatomic species can be calculated in a post-processing step once the atom concentrations are known, with the assumption that the diatomic species are always at chemical equilibrium with each other.

In this section, we present our assumptions on the chemical kinetics and physics involved in the transport mechanism occurring in the gas and solid phases, and at the gas-solid interface. We also derive expressions of gas concentrations and reaction rates as function of the hydrogen atom concentration.

3.1 Gas Phase Species

This work builds on the assumption that the temperature T is constant throughout the column, and the total concentration C_g of all gas atoms is calculated according to the ideal gas law:

$$C_g = 2P/R_gT \tag{1}$$

R_g being the ideal gas constant and P is the gas pressure. C_g is about 82 mM at room

temperature and atmospheric pressure. It is also assumed that no gas properties such as viscosity and diffusivity are composition-dependent.

When determining the concentrations of diatomic species, the enthalpy of formation of the mixed-isotope species is assumed to be zero. In that case, the atoms combine as if they were drawn out of a hat in pairs. If the hat contains equal numbers of H and D atoms, two combinations form the single mixed-isotope species that can be denoted DH or HD, and one each form H_2 and D_2, so their ratio will be 2:1:1. More generally, the diatomic gases will obey the equilibrium relationship

$$K_{\mathrm{HD}} = \frac{[\mathrm{HD}]^2}{[\mathrm{H_2}][\mathrm{D_2}]} = 4 \tag{2}$$

where the brackets indicate the concentration of each species, and K_{HD} is the equilibrium constant. This corresponds to the chemical reaction:

$$\mathrm{H_2} + \mathrm{D_2} \Leftrightarrow 2\mathrm{HD} \tag{3}$$

The following relationship accounts for the hydrogen atoms in the diatomic species, where H is the concentration of hydrogen atoms:

$$2[\mathrm{H_2}] + [\mathrm{HD}] = \mathrm{H} \tag{4}$$

The diatomic species expressions sum to $C_g/2 = P/R_gT$, the total concentration of diatomic molecules in the gas phase such that:

$$[\mathrm{H_2}] + [\mathrm{D_2}] + [\mathrm{HD}] = C_g/2 \tag{5}$$

The number of deuterium atoms is the difference between C_g and H. The diatomic species concentrations can be calculated from C_g and H by summing the number of each type of atom in each diatomic species, and incorporating the equilibrium expression; that is, by

solving Eqs 2,4 and 5 above, which results in:

$$[\mathrm{H}_2] = \frac{\mathrm{H}^2}{2C_g} \tag{6}$$

$$[\mathrm{D}_2] = \frac{(C_g - \mathrm{H})^2}{2C_g} \tag{7}$$

$$[\mathrm{HD}] = \mathrm{H}\left(1 - \frac{\mathrm{H}}{C_g}\right) \tag{8}$$

For the remainder of this paper, H will be used to denote the eluent gas atoms, and HD to denote the mixed-isotope diatomic gas, although no assumptions are made that are specific to these isotopes. Any reference to eluate atoms as D will be without italics to avoid confusion with diffusivities.

3.2 Solid Phase Species

The total concentration of hydrogen isotopes in the solid phase is assumed to be a constant, C_s, with the eluent isotope denoted by H_s and the eluate by $\mathrm{D}_s = C_s - \mathrm{H}_s$. In palladium hydride at room temperature under $P = 1$ atm, C_s is about 70 M; this value is used here. Known variations in C_s with temperature, pressure, and isotopic composition are usually within about 10 percent, as long as the gas pressure is maintained above the transition to the dehydrided state [26].

3.3 Solid-Gas Interface Reaction

The exchange reaction between one isotope in the gas phase and another in the solid phase has been formulated previously by Foltz and Melius using diatomic gas-phase species [22] but it is simpler to consider in monatomic form. It can be written as:

$$\mathrm{H} + \mathrm{D}_s \Leftrightarrow \mathrm{H}_s + \mathrm{D} \tag{9}$$

where the subscript indicates an atom in the solid hydride phase, and no subscript indicates an atom in the gas phase. The net reaction rate R is the forward reaction rate minus the reverse reaction rate:

$$R = \alpha k \frac{\mathrm{H}}{C_g}\left(1 - \frac{\mathrm{H}_s}{C_s}\right) - k\frac{\mathrm{H}_s}{C_s}\left(1 - \frac{\mathrm{H}}{C_g}\right) \tag{10}$$

If k is a rate constant ($k = 20$ mol/m^2.s), R is a flux of H from the gas into the solid. α is the equilibrium constant, also known in this context as the separation factor:

$$\alpha = \frac{\mathrm{H}_s \cdot \mathrm{D}}{\mathrm{H} \cdot \mathrm{D}_s} \tag{11}$$

for concentrations measured at equilibrium [25–27]. It reflects whether H or D is more stable in the solid phase; it is greater than 1 in the former case. In this paper, we assume a constant $\alpha = 2$.

The rate law states that a reaction occurs if a gas atom collides with a solid-phase hydrogen atom at the surface with the necessary configuration to cause a reaction according to Eq. 9 (as reflected by k) multiplied by the probability that the pair is the right isotopic combination for a forward or reverse reaction. The reaction is at equilibrium when $R = 0$; the equilibrium constant can be derived from this case. At the level of detail applied here, the reaction could equivalently take place not as a direct gas-solid collision of hydrogen atoms, but mediated through a surface hydride state.

4 Mathematical Model Formulation

Throughout this section T is the temperature, assumed to be constant throughout the column, and R_g is the ideal gas constant. We assume that the H species is transported in the gas by both advection and diffusion, and by only diffusion in the solid phase.

4.1 Hydrogen Gas Flow and Transport

The hydrogen gas flow in the voids Ω_g of the geometries described in Section 2 is assumed to be laminar with low compressibility [28] (the Mach number is less than 0.3). We also assume that the velocity field does not change in time such that the flow can be described with the following stationary Navier-Stokes equations.

$$\begin{aligned} \nabla \cdot (\rho \boldsymbol{u}) &= 0 \\ \rho(\boldsymbol{u} \cdot \nabla)\boldsymbol{u} &= \nabla \cdot \left[-P\boldsymbol{I} + \mu \left(\nabla \boldsymbol{u} + (\nabla \boldsymbol{u})^T \right) - \frac{2}{3}\mu(\nabla \boldsymbol{u})\boldsymbol{I} \right] \end{aligned} \tag{12}$$

where $\boldsymbol{u}$ is the velocity vector, P is the pressure, μ is the viscosity and $\boldsymbol{I}$ is the identity matrix. The gas density ρ is C_g times the molecular weight of hydrogen. Pressure and concentration are coupled by the ideal gas law (Eq. 1). The inlet is at $z = 0$ where $P = P_{atm} + \Delta P$, and the outlet is at $z = L$ where $P = P_{atm}$, where P_{atm} is the atmospheric pressure and ΔP is the pressure difference between the column inlet and outlet. $\Delta P/P$ is small in this work due to the low flow resistance of the channels. All the other boundaries of Ω_g are considered to be no-slip walls.

Hydrogen transport in Ω_g by convection and diffusion is described by the following PDE:

$$\frac{\partial \mathrm{H}}{\partial t} = \nabla \cdot (D_g \nabla \mathrm{H} - \mathrm{H}\boldsymbol{u}) \tag{13}$$

where H is the hydrogen atomistic concentration and D_g is the gas diffusion coefficient. Initially, a very low concentration H=0.025 mM is assumed in Ω_g except at the inlet $z = 0$ where the concentration is set as H= $2P/R_gT$. At the column output $z = L$, a no-diffusive flux boundary condition is set.

At the solid-gas interface Γ_{sg} a flux boundary condition is applied such that:

$$(D_g \nabla \mathrm{H} - \mathrm{H}\boldsymbol{u}) \cdot \boldsymbol{n}_g = -R \tag{14}$$

where $\boldsymbol{n}_g$ is the vector normal to Γ_{sg} and pointing toward the solid phase and R is the reaction term given in Eq. 10.

4.2 Solid Phase Diffusion

Hydrogen diffusion in Ω_s is described by the following PDE:

$$\frac{\partial \mathrm{H}_s}{\partial t} = \nabla \cdot (D_s \nabla \mathrm{H}) \tag{15}$$

where H_s is the hydrogen atomistic concentration in the solid and D_s is the diffusion coefficient. At the column inlet $z = 0$ and output $z = L$ a no-flux boundary condition is set. Initally, a very low concentration $\mathrm{H}_s = C_s/100$ mM is assumed in Ω_s. At the solid-gas interface Γ_{sg} a flux boundary condition is applied such that:

$$D_s \nabla \mathrm{H} \cdot \boldsymbol{n}_s = R \tag{16}$$

where $\boldsymbol{n}_s$ is the vector normal to Γ_{sg} and pointing toward the gas phase and R is the reaction term given in Eq. 10.

5 Chemical and Physical Parameters

Many of the parameters in the equations above can be estimated from independent information. We assume a diffusivity $D_g = 1$ cm^2/s in the gas phase. The diffusivity is expected to be inversely proportional to total gas concentration [28], but in this work, the concentration variations are small, so this is neglected. The diffusivity D_s of a hydride species within a solid phase is much lower than that of a gas-phase species. We assume that D_s is inversely proportional to the maximum solid phase concentration such that:

$$D_s = D_g \frac{C_{g,0}}{C_s} \tag{17}$$

where $C_{g,0}$ is the maximum gas concentration. Thus, we get $D_s = 1.16 \times 10^{-7}$ cm^2/s which is close to previously reported values [29]. Other physical properties of the hydrogen gas are obtained from [30]. Most notably, we assume a constant gas viscosity $\mu = 8.93 \times 10^{-6}$ Pa.s.

6 Numerical Implementation

The governing equations described above were solved using the commercial finite element software, COMSOL 5.2a. The equations can also be solved using other PDE finite element solvers. Linear elements were used to discretize the PDEs in both Ω_g and Ω_s. The total number of tetrahedral and prism elements is 2.6 and 4.8 million for the geometries considered in our study (top left and bottom right panels of Figure 1, respectively) such that the total number of degrees of freedom is 2.5 and 6 million. For both geometries, the mesh sensitivity was checked by halving the mesh size and verifying that there is a negligible change in the results. The Navier-Stokes equations were solved at steady state to obtain the velocity field in Ω_g. An implicit scheme was used to integrate the transient system of PDEs for the H species diffusion and advection in Ω_g and Ω_s.

7 Results

Our goal in this study was to assess the performance of a 3D structured gas exchange column compared to a simpler column consisting of parallel tubes. We also investigated the effect of defects that could arise during the column manufacturing process. We first report some of the primitive variables computed by our coupled gas flow and diffusion-convection-reaction described in Section 4.

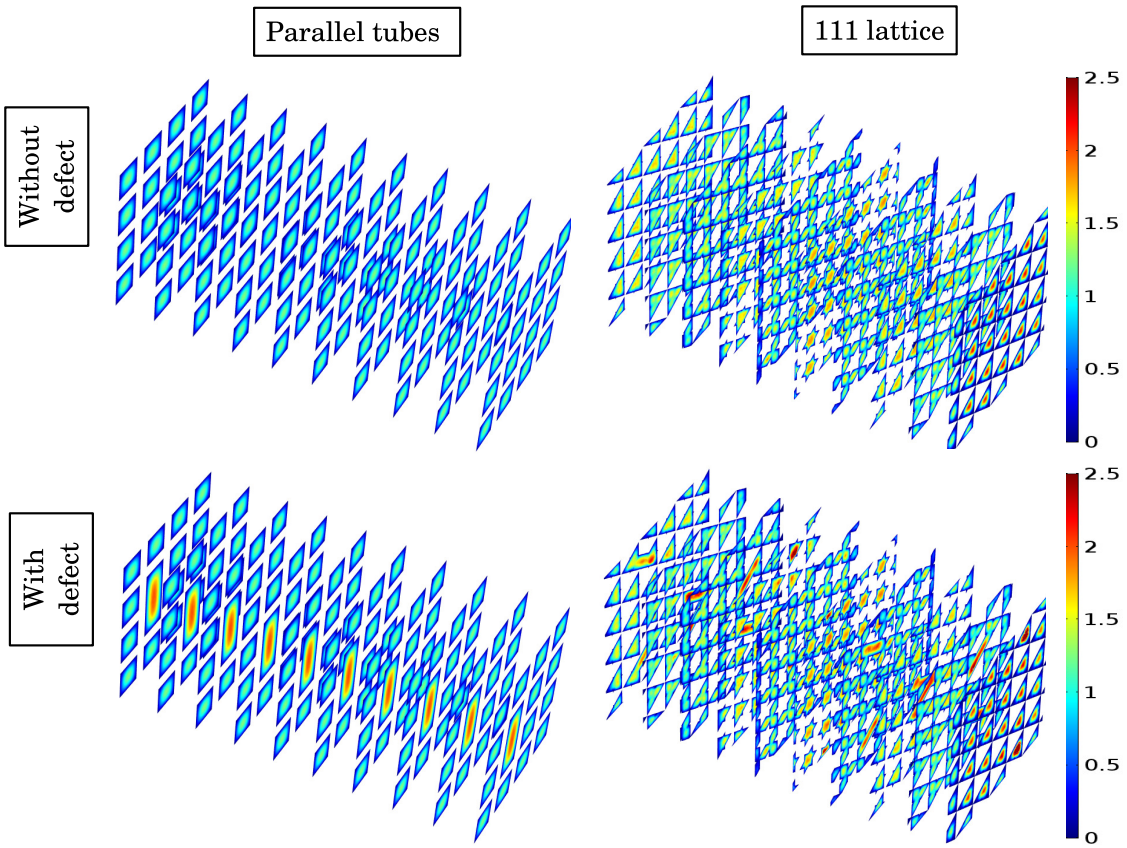

Figure 3: Slice plots normal to the gas flow direction of the velocity profile (in m/s) inside the column for the two column geometries shown in Figure 1, for the cases with and without a defect in the column, as indicated. The column inlet is located at the left-hand side for each panel. Results are generated at the same time step $t = 6.4$s for cases with a total gas flow rate of about 1.5×10^{-4} mol/s.

Figure 3 shows the local velocity profiles in both column geometries described in Section 2 with and and without a defect. The fields resulted from imposing a pressure difference of ΔP=3.5 Pa and ΔP=40 Pa to the parallel tubes and 111 lattice column, respectively. The 111 lattice requires a larger pressure difference to obtain an average velocity similar to the parallel tubes column due to its increased hydraulic resistance. The velocity field is perfectly symmetric and uniform along the column made of parallel tubes, as expected. The velocity is locally increased about two-fold in the presence of a

missing-wall defect in the parallel tubes. In the 111 lattice geometry, the velocity is locally symmetric in each pore due to the symmetry of the unit cells (see Figure 1). However, the velocity varies along the flow direction since the cross-sectional area of the gas pores varies substantially over small distances, causing accelerations and decelerations in the flow. Moreover the 111 lattice column tortuosity participates in hindering the uniformity of the velocity along the flow direction. These effects are more pronounced when a defect is present in the column as shown in the bottom-right of Figure 3. However, the velocities observed in the defect are not significantly higher than the velocity fluctuations in the defect-free structure.

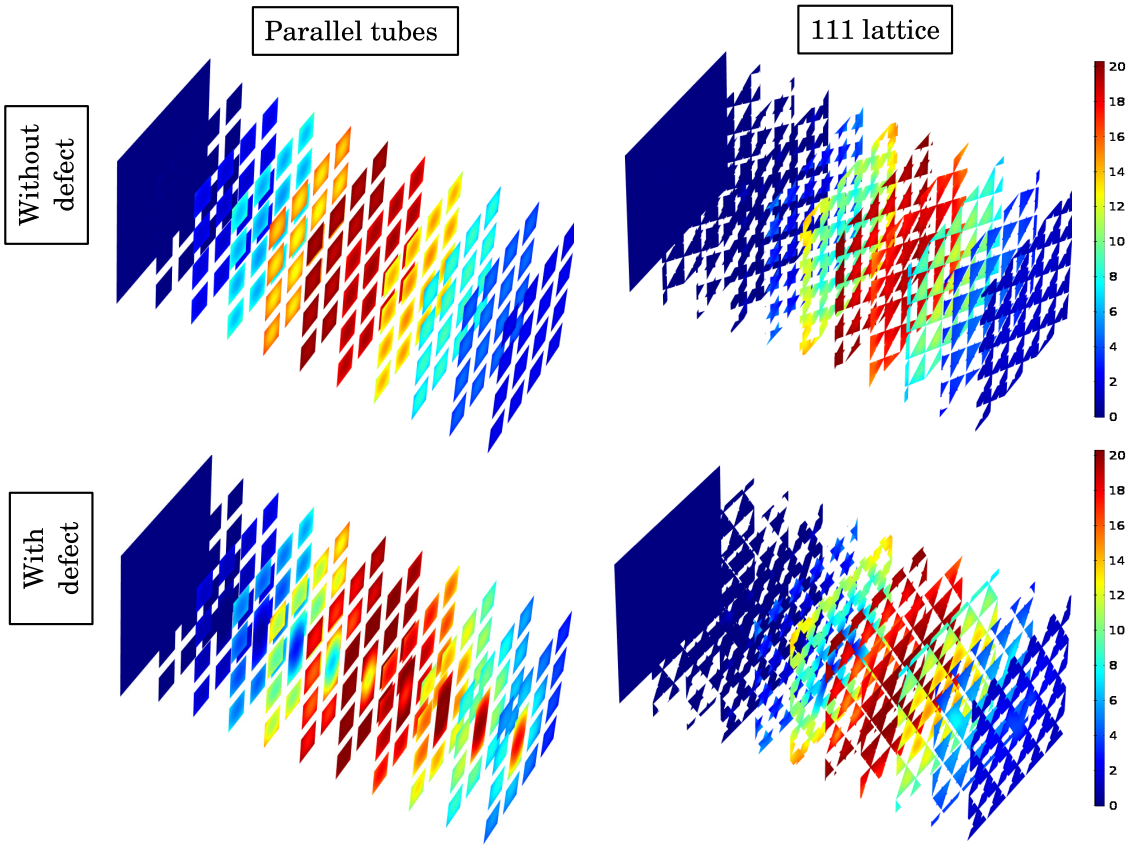

Figure 4: Slice plots normal to the gas flow direction of the HD concentration profile (in mol/m^3) inside the column for the cases shown in Figure 3.

Figure 4 shows the HD species concentration profile, which is a good indicator of the location and size of the reaction front [8]. We notice that there is a gradient in the HD

concentration between the tube wall and center. This effect is less pronounced in the 111 lattice column due to the mixing caused in the tortuous gas flow. In the column region behind the front *i.e.* on the side of the column inlet (left side of the column), the H concentration is larger globally in the column and locally at the center of each tube due to diffusion toward the wall. In that regime, the HD concentration decreases with increasing H (see Eq. 8). Therefore, the HD concentration at the center of each tube is lower than the concentration at the tube walls, as shown. The opposite takes place ahead of the column because the H decreases along the column, and in that regime the HD concentration increases with increasing H. These effects are also less pronounced in the 111 lattice column due to mixing.

For approximately the same total gas flow rate 1.5×10^{-4} mol/s and at a time t=6.4 s where the reaction front is near the middle of the column, the reaction front is narrower in the case of the 111 lattice column than the case of parallel tubes, which is expected since the tortuous structure of the gas path increases the exchange efficiency between the solid and gas phases. The existence of the defect in the parallel tubes geometry significantly distorts the shape and uniformity of the reaction front, as shown in Figure 4 (left panels). The HD gas breaks through the column along the larger tube that results from the absent ligament. On the other hand, there are almost no changes in the front shape and location in the 111 lattice column when a defect is present, as shown in Figure 4 (right panels), despite the significant local increases in the gas velocity observed earlier. In fact, the 111 lattice allows mixing between inhomogeneous regions and prevents major gas break-throughs, maintaining a sharp and stable front.

7.1 Exchange Performance

We measured the performance of the exchange columns with their different geometries considered in our study according to the variation as a function of time of the HD gas concentration at the column outlet. Usually, a narrow HD concentration profile indicates

a sharp front, thus a higher performance. Figure 5 shows the gas species concentrations at the column outlet as a function of time, with results summarized in Table 1.

The table reports t_w, the full width at half-maximum of the HD flow rate profile, and the elution time $t_{elution}$, which is when the reaction front peak exits the column *i.e.*, when the HD flow rate is maximum, for the curves shown in the figure.

The HD concentration at times later than the peak HD flow rate should be equal to zero. This is not the case in the plots shown in Figure 5 and elsewhere in this paper where a small HD residual is obtained at the tail of the distribution. The reason behind this residual is numerical since the mesh is relatively coarse, which allows amplification of the discretization error with time. A finer mesh would eliminate such discrepancies. This was prohibitive in our calculations due to the significant computational costs required by fine 3D meshes.

An approximate total gas flow rate of 1.5×10^{-4} mol/s was established in all cases considered in Figures 3 through 5 by controlling the pressure drop across the column as indicated in the plots. The reaction front indicated by the HD concentration curve is wider in the column with parallel tubes as observed earlier in Figure 4. The ligament defect results in a premature exit of the reaction front in this case due to the HD gas breakthrough in the resulting large tube. However, the existence of a defect has a negligible effect on the exchange performance in the 111 lattice column. The fronts have almost the same width, and exit the column around the same time.

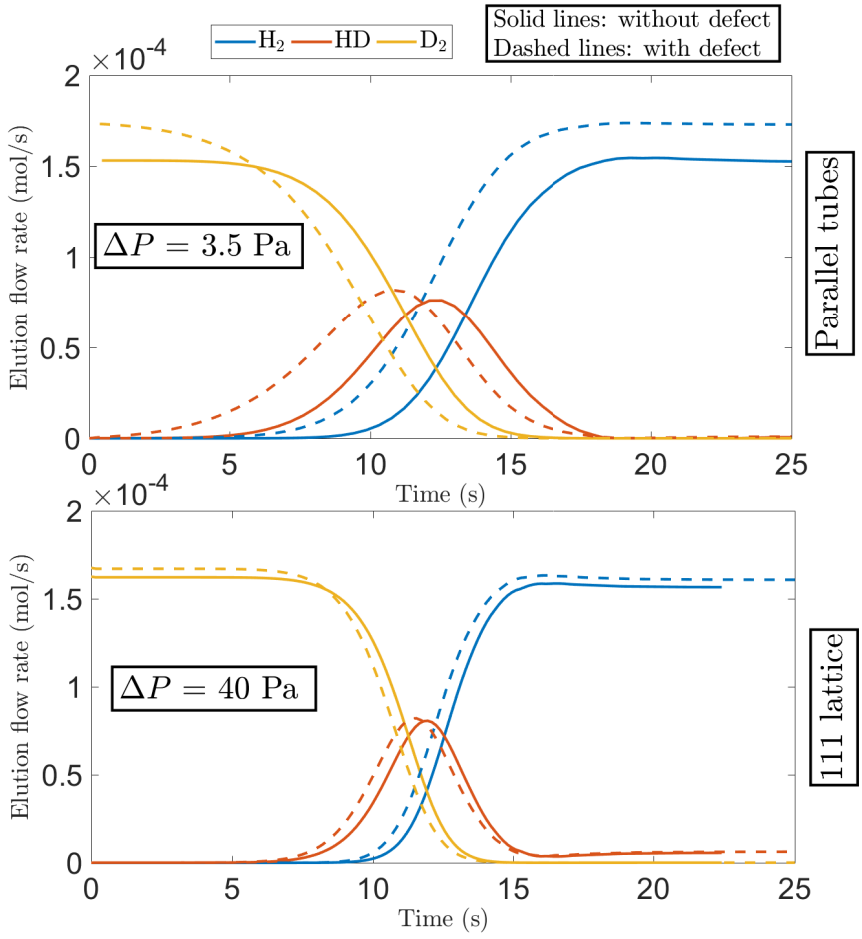

Figure 5: Plots of the hydrogen species flow rates at the column outlet as a function of time for the cases shown in Figure 3.

Table 1: The elution time $t_{elution}$ and peak full width at half maximum t_w of the HD concentration profiles reported for the cases shown in Figure 3. Times shown in parentheses are for cases with a defect.

	Parallel tubes ($\Delta P = 3.5$Pa)	111 lattice ($\Delta P = 40$Pa)
$t_{elution}$ (s)	12.5 (10.83)	11.95 (11.55)
t_w (s)	5.42 (5.73)	3.3 (3.4)

The physical explanation of the shifted peak positions between the dashed and solid curves in Figure 5 is the major difference in gas velocities with and without a defect.

In order to account for the gas velocity, we plot in Figure 6 the gas concentrations as a function of the actual cumulative eluent gas volume $\mathcal{V}$ computed at each time t at the column outlet as:

$$\mathcal{V}_{z=L}(t) = \frac{\frac{1}{2}\int_{\tau=0}^{t}\oint_{\Gamma_g} C_g \boldsymbol{u}\cdot\boldsymbol{n}\, d\Gamma d\tau}{[\mathrm{H_2}]+[\mathrm{HD}]+[\mathrm{D_2}]} \tag{18}$$

where C_g is given by Eq. 1, and $\boldsymbol{u}$ and $\boldsymbol{n}$ are the velocity vector and normal vector, respectively, at the column outlet surface. Here we see that the curves for the cases with and without a defect align with each other and we clearly see that the HD profile *i.e.* reaction front is narrower in a 111 lattice column.

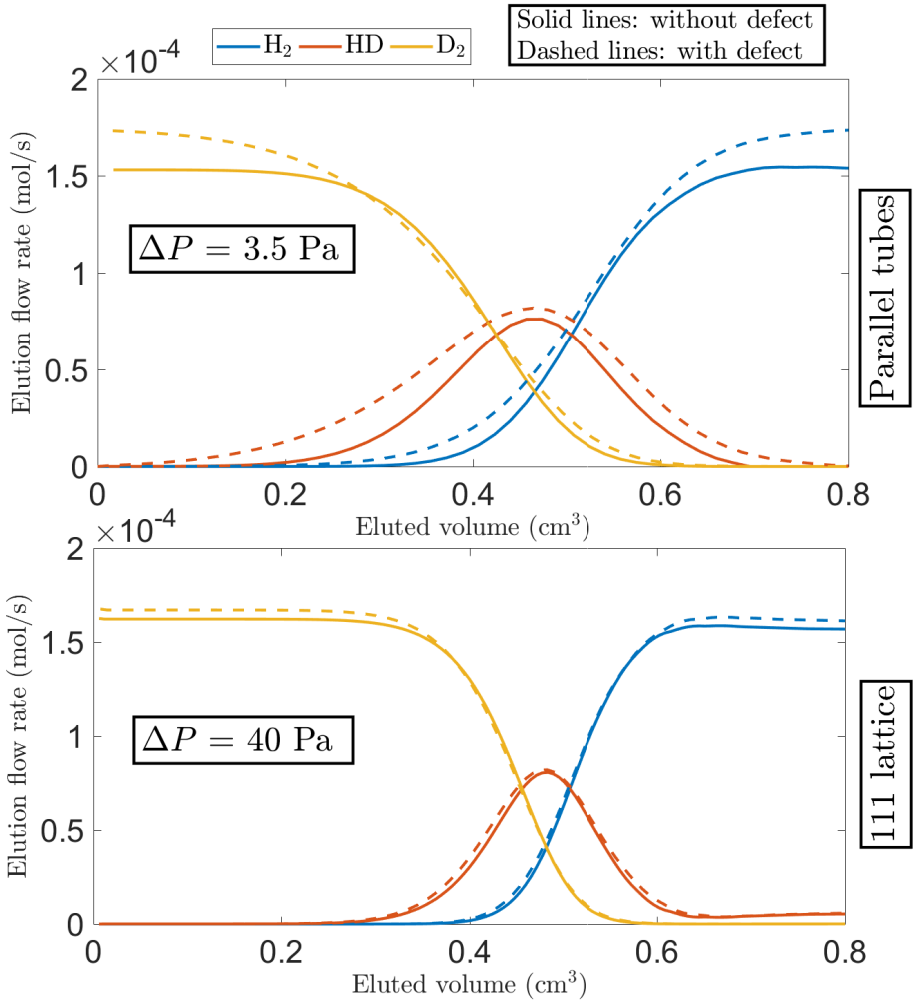

Figure 6: Plots of the hydrogen species flow rates at the column outlet as a function of the actual volume of eluent gas, reported for the cases shown in Figure 3.

Next, we varied the pressure drop in the column and calculated the resulting total gas flow rate. We also computed the number of plates, a performance metric of a chromatography column, which for an exchange chromatography column (where peak width usually does not depend on $\sqrt{L}$) is conveniently defined as:

$$N_p = \frac{t_{elution}}{t_w} \tag{19}$$

When comparing the number of plates to most values in the literature, the expression of N_p in Eq. 19 should be squared to be consistent with the more common definition [31]. The variation of the reduced plate height $1/N_p$ with the Peclet number $Pe = v_0 L_t / D_g = \dot{\mathcal{M}} L_t / (16a^2 D_g C_{g0})$, where $\dot{\mathcal{M}}$ is the molar flow rate and $16a^2$ is the approximate cross-sectional area of Ω_g, is shown in Figure 7 along with the corresponding pressure drops. At low Peclet numbers, *i.e.* low flow rates, the front broadens in the column due to axial diffusion in the gas, resulting in a lower performance. At low Peclet numbers, transport is dominated by axial diffusion, where channel width, and a defect in channel width, do not matter. At large Peclet numbers, reduced performance can result from relatively slow radial diffusion between the center and edge of a tube, slow exchange kinetics, or slow solid-phase diffusion. The limitation present here can be identified as radial diffusion of gas due to the radial concentration gradients shown in Figure 4, along with a similar contribution due to similar gradients in the solid phase.

The peak performance occurs at $\Delta P = 3.5$Pa and $\Delta P = 40$Pa for the parallel tubes and 111 lattice geometries, respectively, which results in a total gas flow rate of 1.5×10^{-4} mol/s. The 111 lattice performance is improved versus the parallel tubes geometry by virtue of the uniform flow mixing strategies included by its construction. However, due to its larger hydraulic resistance, it requires a larger pressure drop to generate the same flow rate as the parallel tubes geometry. Figure 7 also shows the column performance in the case where the defects described previously are present in the column. Relative to the case with no defects, the parallel tube column performance is substantially reduced

in the presence of a defect, whereas that the 111 lattice is more robust to a defect. Fits of the plots to the Van Deemter equation [32] are shown in Table 2, showing parameters for a term proportional to the Peclet number (C) attributable to radial diffusion effects, inversely proportional to the Peclet number (B) attributable to axial diffusion effects, and a term independent of Peclet number (A) traditionally attributed to flow inhomogeneity. A is expected to be zero for an ideal tube geometry, but for a short column, a nonzero value is reasonable. A defect contributes significantly to the A term for the parallel tubes geometry, and much less significantly for the 111 lattice.

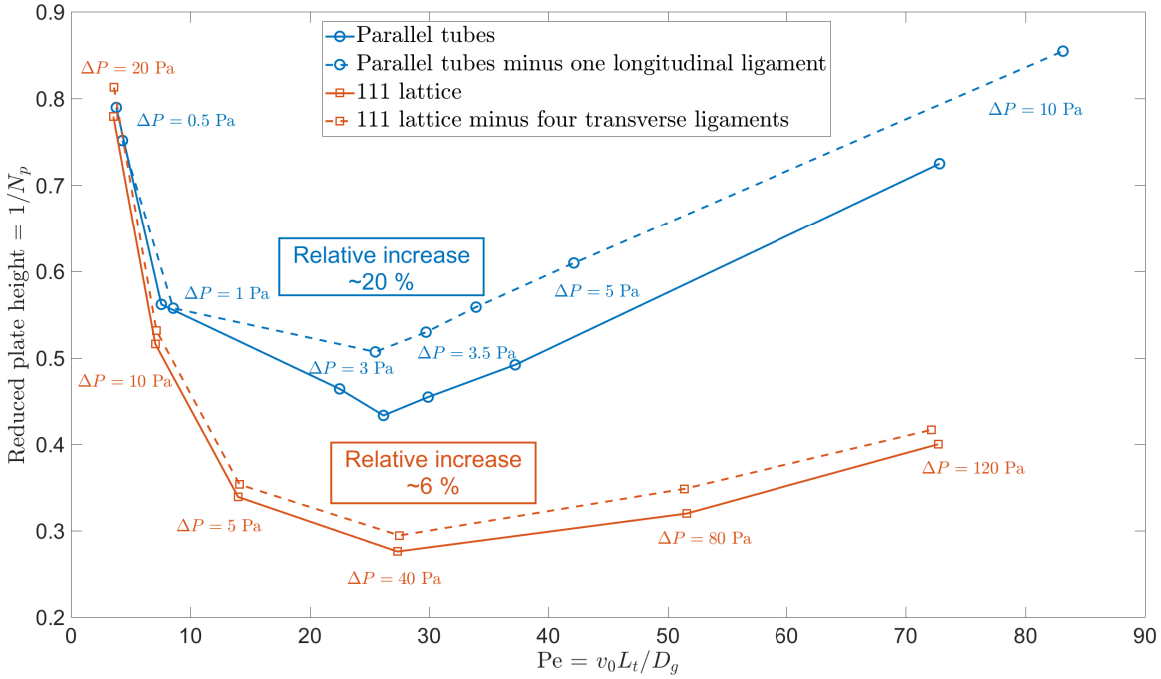

Figure 7: Plots of the reduced plate heights as a function of the Peclet number Pe reported for the two column geometries shown in Figure 1 with and without a defect in the column. The Peclet number was varied by varying the pressure difference ΔP across the column, as indicated.

The results in Figure 7 are reported for an equal volume of defects present in the two geometries considered in this paper. We next investigate the situation where many more ligaments were omitted from the 111 lattice.

Plotted in Figure 8 is the 111 lattice column performance in the absence of different

Table 2: Fitted values of the correlation $1/N_p = A + B/Pe + C \cdot Pe$ relating the reduced plate height and Peclet number plotted in Figure 7.

	Parallel tubes ($\Delta P = 3.5$Pa)	111 lattice ($\Delta P = 40$Pa)
A	0.194 (0.265)	0.131 (0.137)
B	2.2 (1.97)	2.306 (2.424)
C	0.0067 (0.0068)	0.003 (0.0033)

numbers of ligaments, along with the parallel tubes geometry performance with only one ligament removed, with pressure drops across the columns corresponding to the peak performance shown in Figure 7 for the defect-free columns. The locations of these ligaments in the domain are depicted in Figure 2. The plot shows the variation of the HD front with the number of missing ligaments. The relative decrease in the front width when only one ligament is removed from the parallel tubes geometry is about 18%, while it is 5.3% or less when many ligaments are removed from the 111 lattice. There is no correlation between the number of omitted ligaments and the relative increase in the front width (shown in parentheses) because the ligaments were not omitted in a regular systematic pattern from the 111 lattice, as shown in Figure 2. The choice of ligament locations was limited in the ability of having a feasible and reasonable computational mesh in the ligament domains. Nevertheless, these results suggest that the 111 lattice remains robust even with 12 omitted ligaments, which corresponds to about 6.5% of the total solid volume.

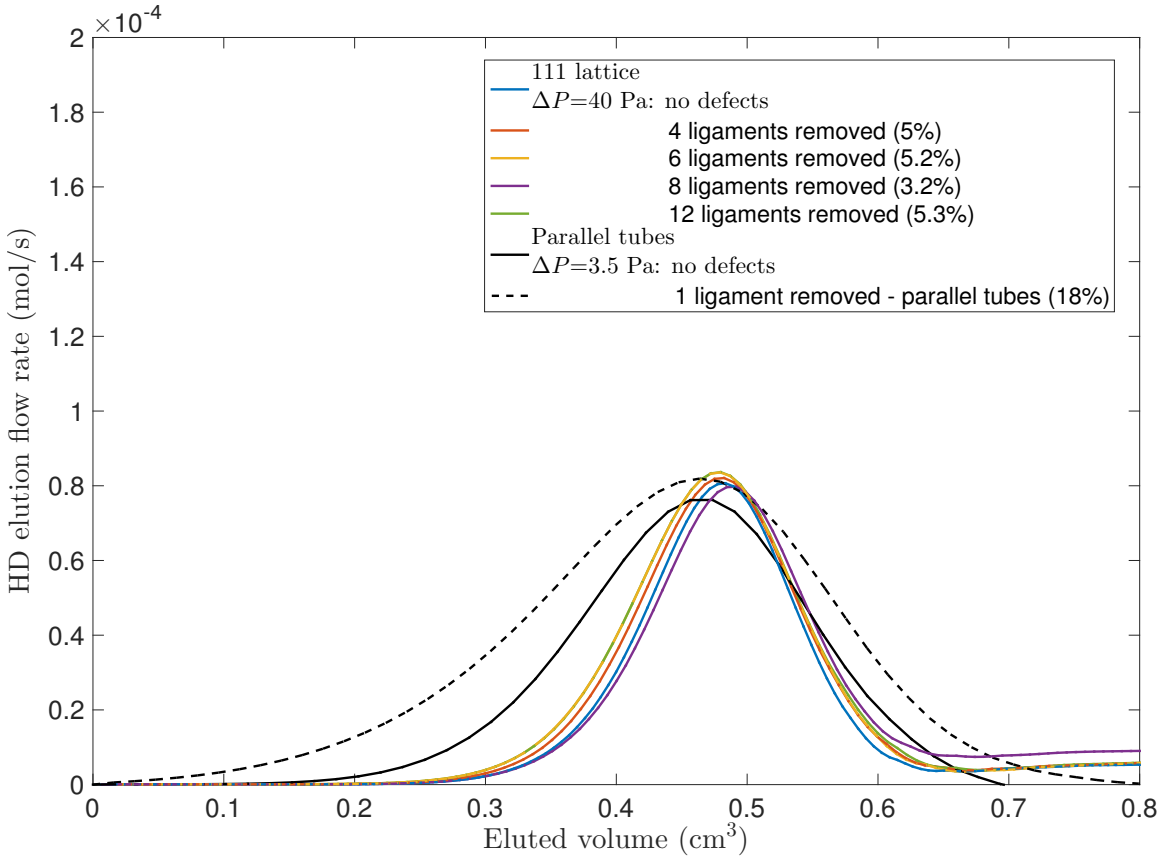

Figure 8: HD elution curves at $\Delta P = 3.5$Pa and $\Delta P = 40$Pa for the parallel tubes and 111 lattice geometries, respectively, where different numbers of ligaments were omitted, as indicated. The percentages shown between parentheses are the relative decrease in the front width.

8 Model Validation

We validated the numerical model for the parallel tubes case by comparing the predicted reaction front spatial width parameter σ computed at half of the elution time with a prediction drawn from an extension of Golay's chromatography theory [3,33] to exchange chromatography. It involves fits to a two-dimensional axisymmetric numerical model of a tube of circular cross section, and is given in [34] for $1 < \alpha < 5$. We report the reduced

plate height σ/L_t in terms of the Peclet number $Pe = v_0 L_t/D_g = \dot{\mathcal{M}} L_t/(16a^2 D_g C_{g0})$ for the parallel tubes geometry as:

$$\frac{\sigma}{L_t} = \frac{4}{\alpha - 1}\left(\frac{1.25}{Pe} + \frac{Pe \cdot a}{L_t^2}\left[\frac{D_g C_g}{2\sqrt{\pi}k} + \frac{a(1+\alpha)}{8\pi} + \frac{4a_h(1+\alpha)(2+a_h/a)}{97\pi}\right]\right) \tag{20}$$

where a is the square tube size (see Figure 1, top). $a = 0.0625$ cm in our case. The terms in Eq. 20 correspond to the contribution of axial diffusion, kinetics and radial diffusion, respectively. The version presented here is recast in terms of Peclet number, and defines σ to correspond to Eq. 21 instead of HD peak area or full width at half maximum.

The predicted σ is estimated by fitting the simulated H concentration profile along the flow direction z in the column with the generalized analytical model [4,5] derived for $\alpha > 1$:

$$\mathrm{H} = C_g\left(1 + \exp\left[\frac{4(\alpha-1)(1+k')(z - z_f(t))}{k'\sigma}\right]\right)^{-1} \tag{21}$$

where $k' = C_s/C_g$, z is the axial coordinate and $z_f(t)$ is the reaction front location in the column. We estimate σ by minimizing the square error between the simulated and analytical H profiles at the middle of the column at a time equal to half the elution time. The results shown in Figure 9 show similar behavior between the numerical and analytical reduced plate height defined for this case as σ/L_t, for a range of Peclet numbers. Discrepancies at larger Peclet numbers may be because the assumption of circular channel cross section in Eq. 20 is oversimplified. At very low Peclet number, when the reduced plate height exceeds 1, it can be difficult to achieve an unambiguous fit to Eq. 21 and σ is very sensitive to Pe, so discrepancies in this range are less significant. The Van Deemter parameters A, B, and C shown in Figure 9 for the simulations are slightly higher than those in Table 2 mainly due to the different definition of peak width used for comparison to the analytical model.

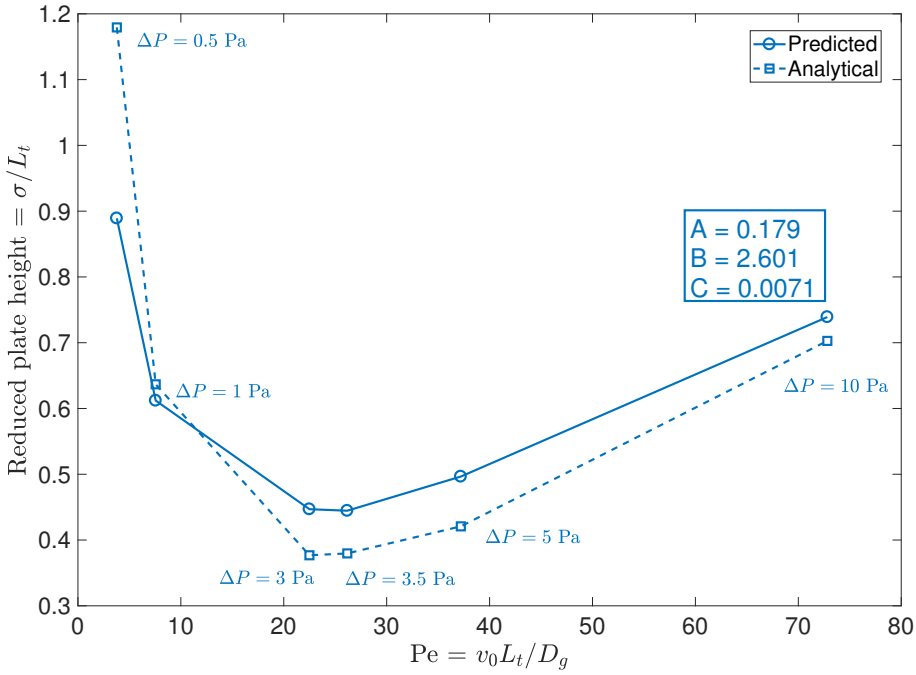

Figure 9: Plots showing the reduced plate height predicted by the 3D numerical model and by Eq. 20 corresponding to the flow in the parallel tubes geometry shown in Figure 1 (top), as a function of the Peclet number Pe. Van Deemter parameters A, B, and C are reported for the numerical model.

9 Conclusion

In this paper, we have proposed a deterministic geometry having a 3D structure to be used in chromatography applications in order to avoid disadvantages of one-dimensional tube arrays and complications of packed-powder beds. The geometry we propose is drawn along the 111 direction of a regular cubic 3D lattice and is well suited to fabrication by additive manufacturing technologies. We have also developed a simplified numerical hydrogen isotope exchange model to study the performance of the proposed geometry compared to that of 1D parallel tubes. The model results are in approximate agreement with results obtained for a simpler 2D model. For the same flow rate, the performance

quantified by the number of plates of our proposed 3D structure geometry is improved versus that of the parallel tubes geometry. Moreover, the 3D structure geometry is more robust to manufacturing defects than the parallel tubes geometry. By allowing flow shuffling and mixing, our proposed geometry is robust to defects occupying up to 6% of the total solid bed volume. The results presented here suggest that efforts to manufacture chromatography columns with a deterministic network of three-dimensional flow channels are likely to be worthwhile, yielding improvements over simpler column structures like arrays of one-dimensional tubes. Understanding of these improvements would be further advanced by development of models of packed powders suitable for comparison, consideration of sensitivity to other types of defects, and validation by comparison to experimental results.

10 Acknowledgements

This contribution was identified by Norman Loney (New Jersey Institute of Technology) as the Best Presentation in the session "Mathematical Modeling of Transport Processes" of the 2016 AIChE Annual Meeting in San Francisco.

This work was supported by the Laboratory-Directed Research and Development program at Sandia National Laboratories, a multi-mission laboratory managed and operated by National Technology and Engineering Solutions of Sandia, LLC., a wholly owned subsidiary of Honeywell International, Inc., for the U.S. Department of Energys National Nuclear Security Administration under contract DE-NA-0003525.

11 References

[1] Walter J.E. Multiple adsorption from solutions. *J. Chem. Phys.*, 13(6):229–235, 1945. 2

[2] H.C. Thomas. Heterogeneous ion exchange in a flowing system. *J. Am. Chem. Soc.*, 66(10):1664–1666, 1944. 2

[3] Golay M.J.E. Theory of chromatography in open and coated tubular columns with round and rectangular cross sections. In *Gas Chromatography 1958: Proceedings of the Second Symposium*, pages 36–55, 1958. 2, 3, 25

[4] Vermeulen T. Separation by adsorption methods. In Drew T.B. and Hoopes J.W. Jr, editors, *Advances in Chemical Engineering*, volume II, pages 147–208, 1958. 2, 26

[5] Robinson D.B. Hydrogen isotope exchange in a metal hydride tube. Technical report, Sandia National Laboratories, Albuquerque, NM, 2014. SAND2014-17174, download from osti.gov. 2, 9, 26

[6] Billen J. and Desmet G. Understanding and design of existing and future chromatographic support formats. *J. Chromatogr. A.*, 1168:73–99, 2007. 2, 3

[7] Kolasinski R.D., Shugard A.D., Tewell C.R., and Cowgill D.F. Uranium for hydrogen storage applications: A materials science perspective. Technical report, Sandia National Laboratories, Albuquerque, NM, 2010. SAND2010-5195, DOI: 10.2172/993617. 2

[8] Powell G.L. and Kirkpatrick J.R. Effects of surface thermodynamics on hydrogen isotope exchange kinetics in palladium: Particle and flow models. *Chem. Eng. Sci.*, 122:474–490, 2015. 2, 17

[9] Fichou D. and Morlock G.E. Open-source-based 3D printing of thin silica gel layers in planar chromatography. *Anal. Chem.*, 89(3):2116–2122, 2017. 3

[10] DR Reyes, D Iossifidis, PA Auroux, and A Manz. Micro total analysis systems. 1. Introduction, theory, and technology. *Anal. Chem.*, 74(12):2623–2636, 2002. 3

[11] Femmer T., Flack I., and Wessling M. Additive manufacturing in fluid process engineering. *Chemie Ingenieur Technik*, 88(5):535–552, 2016. 3

[12] Waheed S., Cabot J.M., Macdonald N.P., Lewis T., Guijt R.M., Paull B., and Breadmore M.C. 3D printed microfluidic devices: enablers and barriers. *Lab. Chip.*, 16:1993–2013, 2016. 3

[13] Wei M., Zhang F., Wang W., Alexandridis P., Zhou C., and Wu G. 3D direct writing fabrication of electrodes for electrochemical storage devices. *J. Power. Sources.*, 354:134–147, 2017. 3

[14] Schisla D.K., Ding H.B., Carr P.W., and Cussler E.L. Polydisperse tube diameters compromise multiple open-tubular chromatography. *AIChE J.*, 39(6):946–953, 1993. 3, 4

[15] Gzil P., Baron G.V., and Desmet G. Computational fluid dynamics simulations yielding guidelines for the ideal internal structure of monolithic liquid chromatography columns. *J. Chromatogr. A.*, 991:169–188, 2003. 3

[16] Desmet G., Callewaert M., Ottevaere H., and De Malsche W. Merging open-tubular and packed bed liquid chromatography. *Anal. Chem.*, 87:7382–7388, 2015. 3

[17] Su C-K., Peng P-J, and Sun Y-C. Fully 3D-printed preconcentrator for selective extraction of trace elements in seawater. *Anal. Chem.*, 87(13):6945–6950, 2015. 3

[18] Couck S., Lefevere J., Mullens S., Protasova L., Meynen V., Desmet G., Baron G.V., and Denayer J.F.M. CO_2, CH_4 and N_2 separation with a 3DFD-printed ZSM-5 monolith. *Chem. Eng. J.*, 308:719–726, 2017. 3

[19] Fee C., Nawada S., and Dimartino S. 3D printed porous media columns with fine control of column packing morphology. *J. Chromatogr. A.*, 1333:18–24, 2014. 3

[20] Nawada S., Dimartino S., and Fee C. Dispersion behavior of 3D-printed columns with homogeneous microstructures comprising differing element shapes. *Chem. Eng. Sci.*, 164:90–98, 2017. 3

[21] Jones C.G., Mills B.E., Nishimoto R.K., and Robinson D.B. Electroless deposition of palladium on macroscopic 3d-printed polymers with dense microlattice architectures for development of multifunctional composite materials. *J. Electrochem. Soc.*, 164(13):D867–D874, 2017. DOI: 10.1149/2.1341713jes. 6

[22] Foltz G. W. and Melius C. F. Studies of isotopic exchange between gaseous hydrogen and palladium hydride powder. *J. Catalysis*, 108:409–425, 1987. 9, 11

[23] Fukada S. Numerical simulation of elution chromatography for separation of H_2-HD-D_2 mixtures using a palladium particle bed. *Separation Sci. Tech.*, 34(14):2699–2721, 1999. 9

[24] Charton S., Corriou J.P., and Schweich D. Modeling of hydrogen isotopes separation in a metal hydride bed. *Chem. Eng. Sci.*, 54:103–113, 1999. 9

[25] Boris M. Andreev and Eldar P. Magomedbekov. Separation of hydrogen isotopes by chemical isotope exchange in system involving metal and intermetallic compound hydrides. *Separation Sci. Tech.*, 36(8-9):2027–2086, 2001. 9, 12

[26] Flanagan T.B. and Oates W.A. The palladium-hydrogen system. *Annual Review of Material Science*, 21(12):269–304, 1991. 11, 12

[27] Luo W., Cowgill D.F., and Flanagan T.B. Separation factors for hydrogen isotopes in palladium hydride. *J. Phys. Chem. C*, 117(27):13861–13871, 2013. 12

[28] R. Byron Bird, Warren E. Stewart, and Edwin N. Lightfoot. *Transport Phenomena*. John Wiley and Sons, New York, 2nd edition, 2002. 13, 14

[29] James S. C., Hamilton J., and Wolfer W.G. Diffusional exchange of isotopes in a metal hydride sphere. *Chem. Eng. Sci.*, 68(1):250–257, 2012. 15

[30] White F.M. *Viscous Fluid Flow*. McGraw-Hill, New York, NY, 3rd edition, 2006. 15

[31] Fukada S., Fuchinoue K., and Nishikawa M. Isotope separation factor and isotopic exchange rate between hydrogen and deuterium of palladium. *J. Nucl. Mat.*, 226(3):311–318, 1995. 22

[32] van Deemter J.J., Zuiderweg F.J., and Klinkenberg A. Longitudinal diffusion and resistance to mass transfer as causes of nonideality in chromatography. *Chem. Emg. Sci.*, 5:271–289, 1956. 23

[33] Clifford A.A. Theory of open-tube chromatography: an exact proof of Golay's equations. *J. Chromatography.*, 471:61–69, 1989. 25

[34] Robinson D.B. Hydrogen isotope exchange in a metal hydride tube. Technical report, Sandia National Laboratories, Albuquerque, NM, 2017. SAND2017-9774, available by request from ntis.gov. 25